CrossMark

ORIGINAL ARTICLE

Visualization of vascular injuries in extremity trauma

Kwitae Chong[1] · Chenfanfu Jiang[2] · Daniel Ram[3] · Anand Santhanam[4] ·
Demetri Terzopoulos[2] · Peyman Benharash[5] · Erik Dutson[5] · Joseph Teran[3] ·
Jeff D. Eldredge[1]

Abstract A tandem of particle-based computational methods is adapted to simulate injury and hemorrhage in the human body. In order to ensure anatomical fidelity, a three-dimensional model of a targeted portion of the human body is reconstructed from a dense sequence of CT scans of an anonymized patient. Skin, bone and muscular tissue are distinguished in the imaging data and assigned with their respective material properties. An injury geometry is then generated by simulating the mechanics of a ballistic projectile passing through the anatomical model with the material point method. From the injured vascular segments identified in the resulting geometry, smoothed particle hydrodynamics (SPH) is employed to simulate bleeding, based on inflow boundary conditions obtained from a network model of the systemic arterial tree. Computational blood particles interact with the stationary particles representing impermeable bone and skin and permeable muscular tissue through the Brinkman equations for porous media. The SPH results are rendered in post-processing for improved visual fidelity. The overall simulation strategy is demonstrated on an injury scenario in the lower leg.

Keywords Injury biomechanics · Hemorrhage simulation · Cardiovascular tree model · Smoothed particle hydrodynamics · Material point method

✉ Kwitae Chong
blueman17@ucla.edu

Chenfanfu Jiang
chenfanfu.jiang@gmail.com

Daniel Ram
chunaleh@gmail.com

Anand Santhanam
ASanthanam@mednet.ucla.edu

Demetri Terzopoulos
dt@cs.ucla.edu

Peyman Benharash
PBenharash@mednet.ucla.edu

Erik Dutson
EDutson@mednet.ucla.edu

Joseph Teran
jteran@math.ucla.edu

Jeff D. Eldredge
eldredge@seas.ucla.edu

[1]   Mechanical and Aerospace Engineering, University of California, Los Angeles, Los Angeles, CA 90095, USA

[2]   Computer Science, University of California, Los Angeles, Los Angeles, CA 90095, USA

[3]   Mathematics, University of California, Los Angeles, Los Angeles, CA 90095, USA

[4]   Radiation Oncology, University of California, Los Angeles, Los Angeles, CA 90095, USA

[5]   Surgery, University of California, Los Angeles, Los Angeles, CA 90095, USA

1 Introduction

Medical training for both trauma care and surgery, in both military and civilian contexts, is currently evolving toward a

paradigm that relies on virtual representations of injuries and treatment [3, 4, 6, 11, 17, 18, 20]. Training systems based on an interactive and anatomically realistic model of an injury on a computing platform have the potential to substantially reduce, or eliminate altogether, the loss of animals that serve as the basis of the current training paradigm and to enhance the learning opportunities when coupled with state-of-the-art adaptive learning tools [15, 16]. In the past decade, there have been notable advances in the development of techniques for real-time rendering of deformable models of the human physiology [6, 17, 20]. However, these models generally lack a representation of bleeding, in part because the governing equations of hemodynamics are inherently nonlinear and, thus, require substantially more computational complexity than modeling of solid materials such as tissue.

In this work, we propose a set of methodologies for the virtual simulation of traumatic injury and subsequent hemorrhaging. Rather than attempt to achieve real-time levels of computational efficiency, we focus here on achieving visual fidelity and establishing the underlying workflow on a representative injury to the lower leg. This workflow starts from construction of the anatomical model from segmentation of CT scans. The anatomical model is virtually injured through numerical simulation of the bone, muscle tissue and skin mechanics with the material point method (MPM) [32]. This method, a generalization of the particle-in-cell/fluid implicit particle method to solid mechanics, has recently been shown to be powerful in simulating various materials in the presence of large deformation [14, 25, 29, 30]. As a hybrid particle/grid method, MPM uses an Eulerian grid to handle contact and topology changes while material properties are tracked on Lagrangian particles. These features make it well suited for simulating human body injury where extreme deformation and material damage may occur under large impact forces.

Bleeding simulations are performed on the resulting (static) injured geometry with the method of smoothed particle hydrodynamics (SPH). The SPH method was originally invented to simulate phenomena in astrophysics [12, 19] and has been extended into a variety of physical contexts such as gaseous phenomena [27] and highly deformable bodies [8]. These advances have demonstrated the excellent potential for SPH in multi-scale fluid simulation in computer animation [1, 13, 26]. As a particle-based Lagrangian method, fluid particles interact with neighboring particles via hydrodynamic forces, within an area of influence established by the interpolation kernel. The simple methodology enables easy implementation for high-fidelity fluid simulations. Müller et al. [22] developed an interactive bleeding simulation for virtual surgery with SPH and showed that SPH can be integrated as an essential component into a surgical training system. Here, we extend the use of SPH in this context to couple it with a systemic model of the circulatory system.

In Sect. 2, the anatomical construction and injury and hemorrhage simulation procedures will be described. The procedure for obtaining the inflow boundary conditions to the hemorrhage simulation from a vascular tree model will also be detailed. A pair of visualized hemorrhage simulations in an injured anatomical model of the lower human leg will be examined in Sect. 3. Then, discussion and concluding remarks will follow in Sects. 4 and 5.

2 Methodology

The simulations of hemorrhaging in the injured human body carried out in this work are conducted in three steps. First, the anatomical model is reconstructed as a collection of skin, bone and tissue particles from CT scan images of an anonymized patient. In the next step, the anatomical model is virtually injured by simulating the mechanics of ballistic projectiles passing through the model. Finally, a simulation of bleeding is performed on the static geometry generated by the injury, based on distinct treatments of the interaction of blood particles with skin, bone and tissue particles. The inflow conditions for the bleeding simulation are provided by a coupled one-dimensional vascular tree model. The details of these steps are described below in the context of a simulation of traumatic injury to the lower leg.

2.1 Image segmentation of human anatomical model

The anatomical model for the simulations was constructed through segmentation of a dense series of CT scans. This series was obtained from a whole-body scan of a cancer patient, carried out as part of their regular therapy. It was ensured that the patient chosen was free of cancer in the leg, which is the focus of simulations in the demonstration below. The anatomy was anonymized before its use in subsequent simulations (Fig. 1).

The resolution of the images was 0.75 mm in each lateral slice, and the slices were spaced longitudinally by 4 mm. Contours were manually generated for distinct parts of the anatomy, e.g., limb, torso by a clinical expert, using MIMVista® contouring software. Gaps in the contours were eliminated using spline connections between nearby contour points. The contour slices, obtained from multiple two-dimensional scans, were often at oblique angles with respect to each other. This required a novel contour-guided approach to construct the final volume segmentation.

2.2 Injury generation

The data from the segmentation process described above consist of voxel images in a three-dimensional grid. Each
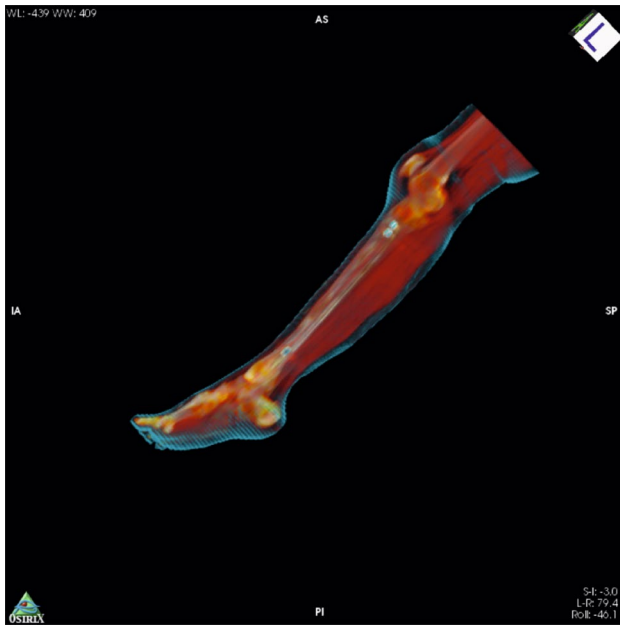
Fig. 1 Final volume segmentation of leg anatomical model

voxel is labeled as skin, bone and internal tissue. Sampling at voxel centers results in an initial collection of particles. Open VDB [23] is used to reconstruct high-resolution level sets from the particle collection. Scan noise is removed by performing a smoothing step on the signed distance fields. New particles are then inserted inside the level sets using Poisson disk sampling [5]. This allows for arbitrary particle resolution and prevents grid-aligned artifacts.

Given the particle samples, the material point method (MPM) is used to simulate the dynamics of a ballistic projectile passing through the anatomical model. The MPM uses particles (i.e., material points) to track Lagrangian quantities, particularly mass, velocity and deformation gradient. The governing equation

$$\rho_s \frac{D\boldsymbol{v}}{Dt} = \nabla \cdot \boldsymbol{\sigma} + \rho \boldsymbol{g} \tag{1}$$

is solved on a background Eulerian grid, where ρ_s is the local material density, $\boldsymbol{v}$ is velocity, $\boldsymbol{\sigma}$ is the Cauchy stress tensor, $\boldsymbol{g}$ is the gravity and D/Dt denotes the material derivative.

Each of the three materials is assigned with its corresponding elasto-plastic constitutive model parameters. This is easily done since stress is essentially computed at individual MPM particles. Using MPM also avoids the need to explicitly model coupling and contact between particles. The external projectile (modeled as a sphere here for simplicity) is kinematically moved and treated as a rigid body collision object during the impact simulation. Dirichlet boundary conditions are applied to the particles near the ends of the model to hold the leg in place.

Fig. 2 Material point method (MPM) simulation of projectile impact. *Yellow*, *red* and *white* particles represent skin, tissue and bone, respectively. The *first column* shows the side view and the *second column* shows the back view (color figure online)

The simulation time scale of the projectile impact is on the order of 1 ms. Sample simulation frames are shown in Fig. 2. Particle positions in the last frame are exported as the injured geometry, as shown in Fig. 3.

Fig. 3 A close view of the injured geometry after the MPM simulation. *Left* front view; *Right* back view
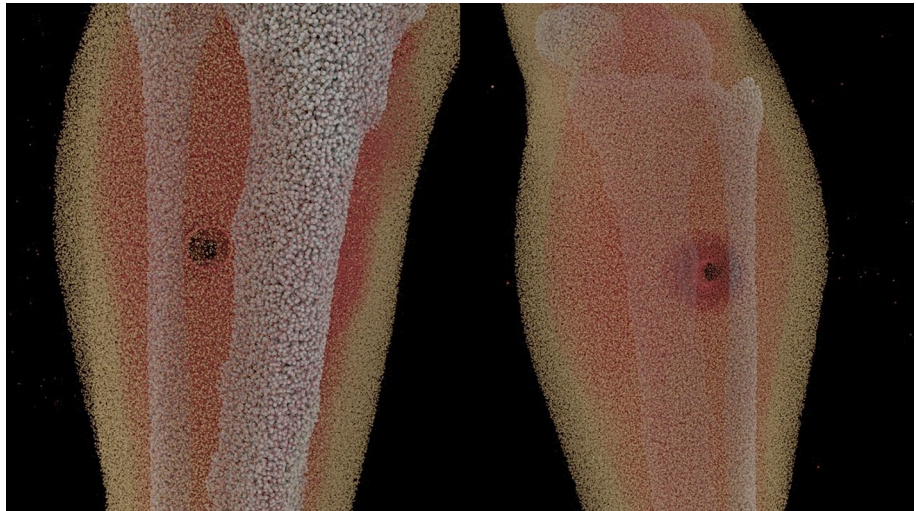
2.3 Hemorrhage simulation

In the static injury geometry generated in the previous step, the method of smoothed particle hydrodynamics (SPH) is employed to simulate the flow of blood. Like MPM, the SPH method is Lagrangian, representing blood as a collection of discrete particles that transport flow properties, such as mass and velocity. The fluid particles interact with each other within a given radius, which leads to a high-fidelity method that converges as the number density of particles increases [7, 24]. Mass conservation is trivially satisfied by ensuring that the mass of each particle is invariant. When in a simple medium (such as air), the transport is governed by the Navier–Stokes equations for incompressible flow,

$$\rho \frac{D\boldsymbol{v}}{Dt} = -\nabla p + \mu \nabla^2 \boldsymbol{v} + \rho \boldsymbol{g}, \tag{2}$$

where ρ and μ are, respectively, the density and dynamic viscosity of blood and p is the pressure. However, in our simulations, soft tissue is treated as a porous medium, in which the transport is modeled by the Brinkman equations [9, 31],

$$\rho \frac{D\boldsymbol{v}}{Dt} = -\epsilon \nabla p + \mu \nabla^2 \boldsymbol{v} + \rho \boldsymbol{g} - \epsilon \frac{\mu}{K} \boldsymbol{v} \tag{3}$$

where ϵ and K denote, respectively, the porosity and permeability of the porous medium. The last term of Eq. (3) represents Darcy's law, which describes the resistance to transport in a porous medium. For muscle tissue, the value of permeability is very small ($K = 5.0 \times 10^{-7}$ m^2). The tissue's local porosity is inversely related to the local density of muscle tissue, which is determined from the set of computational particles representing this tissue. This accounts for inhomogeneity of transport

within the muscle tissue, particularly in regions damaged by the injury. It should be noted that the Navier–Stokes equations are recovered by setting the permeability to very large value and the porosity to unity. Thus, the Brinkman equation (3) is used to govern all fluid motion in the simulations reported here.

The Brinkman equations are discretized by interpolating field quantities with the set of SPH particles. This interpolation is carried out by a weighted summation over the particles within a local neighborhood whose size is established by the smoothing radius, h, of a smoothing kernel, W. For example, a generic field quantity, $A(\boldsymbol{r})$, is obtained by summing over particles j,

$$A(\boldsymbol{r}) = \sum_j A_j \frac{m_j}{\rho_j} W(\boldsymbol{r} - \boldsymbol{r}_j, h), \tag{4}$$

where A_j, m_j and ρ_j denote, respectively, the quantity A, mass and density carried by particle j, and $\boldsymbol{r}_j$ represents its position. In this work, the smoothing kernel is given by

$$W(\boldsymbol{r}, h) = -\frac{315}{64\pi h^9} \left(h^2 - |\boldsymbol{r}|^2 \right)^3, \tag{5}$$

for all $|\boldsymbol{r}| < h$. That is, only particles within the smoothing radius are included in the summation in (4). The density of any particle i is computed from a weighted average of particle masses via (4), omitting the influence of the particle itself,

$$\rho_i = \sum_{j \neq i} m_j W(\boldsymbol{r}_i - \boldsymbol{r}_j, h). \tag{6}$$

The pressure is obtained from the density by a modified form of the ideal gas equation of state [8],

$$p_i = k(\rho_i - \rho_0), \tag{7}$$

where ρ_0 is the density of the fluid at stationary condition and k is a gas constant. This pressure implementation leads to a weakly compressible flow, within which pressure acts as an attractive force for relatively lighter fluid density and repulsive force for relatively heavier fluid density, thereby enabling the maintenance of a reasonably uniform density field.

From Eq. (4), the gradient and Laplacian of a field quantity can be obtained by applying these operations directly to the smoothing kernel. In particular, the gradient and Laplacian of A at the location of particle i are, respectively,

$$\nabla A_i = \sum_{j \neq i} A_j \frac{m_j}{\rho_j} \nabla W(\boldsymbol{r_i} - \boldsymbol{r_j}, h), \tag{8}$$

and

$$\nabla^2 A_i = \sum_{j \neq i} A_j \frac{m_j}{\rho_j} \nabla^2 W(\boldsymbol{r_i} - \boldsymbol{r_j}, h). \tag{9}$$

These forms are applied to discretize the terms in (3), but with different specialized smoothing kernels applied to the pressure and viscous terms. Specifically, the pressure, viscous, gravity and Darcy forces acting on particle i are, respectively, modeled by

$$\boldsymbol{f}_i^p = \epsilon \rho_i \sum_{j \neq i} \left(\frac{p_i}{\rho_i^2} + \frac{p_j}{\rho_j^2} \right) m_j \nabla W_p(\boldsymbol{r_i} - \boldsymbol{r_j}, h), \tag{10}$$

$$\boldsymbol{f}_i^v = \mu \sum_{j \neq i} (\boldsymbol{v_j} - \boldsymbol{v_i}) \frac{m_j}{\rho_j} \nabla^2 W_v(\boldsymbol{r_i} - \boldsymbol{r_j}, h), \tag{11}$$

$$\boldsymbol{f}_i^g = \rho_i \boldsymbol{g}, \tag{12}$$

$$\boldsymbol{f}_i^d = -\epsilon \frac{\mu}{K} \boldsymbol{v_i}, \tag{13}$$

where $\nabla W_p(\boldsymbol{r}, h) = -\frac{45}{\pi h^6} \frac{\boldsymbol{r}}{|\boldsymbol{r}|} (h - |\boldsymbol{r}|)^2$ and $\nabla^2 W_v(\boldsymbol{r}, h) = \frac{45}{\pi h^6} (h - |\boldsymbol{r}|)$ denote, respectively, the gradient of the smoothing kernel used for the pressure force

and the Laplacian of the smoothing kernel used for the viscous force. The smoothing kernel for pressure, W_p, is designed to prevent particle clustering and dilution, whereas the viscous smoothing kernel, W_v, ensures positive viscous diffusion [21]. Pressure and viscous forces are constructed to maintain symmetry of force in binary particle interactions so that global conservation of momentum is ensured. The local values of porosity and permeability are determined by the MPM tissue particles in the injured geometry.

Bone and skin are treated as impenetrable materials in the bleeding simulations within the injured geometry. It is important to stress that rigorous enforcement of these constraints would be computationally intensive, requiring continuous inspection for overlaps between blood particles and the geometrically complex interfaces formed between bone or skin and the adjacent media. Instead, we include the bone and skin particles from the MPM simulation results as stationary particles within the SPH simulation, and their impenetrability is enforced approximately through the pressure force they exert on convecting blood particles. This approach was verified through simulations (omitted for brevity) of the canonical problem of sloshing within a rectangular vessel.

Blood particles in the SPH simulation are continuously introduced into the physical domain on a spherical shell of small radius, 0.0015 m, centered within the injury site. These newly introduced particles are initialized with a velocity directed radially outward from the center of the sphere, with magnitude based on the instantaneous volume flow rate for the injury, $Q_{inj}(t)$. This volume flow rate is determined from a one-dimensional distributed parameter model of the arterial tree [2, 28] that includes 91 arterial segments, each described by a characteristic impedance based on the Womersley flow (pulsatile flow of viscous fluid in an elastic vessel) [33]. The properties of the arteries are based on tabulated values by Stergiopulos et al. [28]. At the site of an injury in this tree, the injury arterial segment is shunted with an 'injury branch' of low impedance [10]. The pressure at the outlet of this

Fig. 4 (*Left*) Single cardiac cycle of the pressure signal in the aorta (*dashed line*) and in the injured left anterior tibial artery (*solid line*). (*Right*) Initial rate of blood loss through the severed left anterior tibial artery, during one cardiac cycle
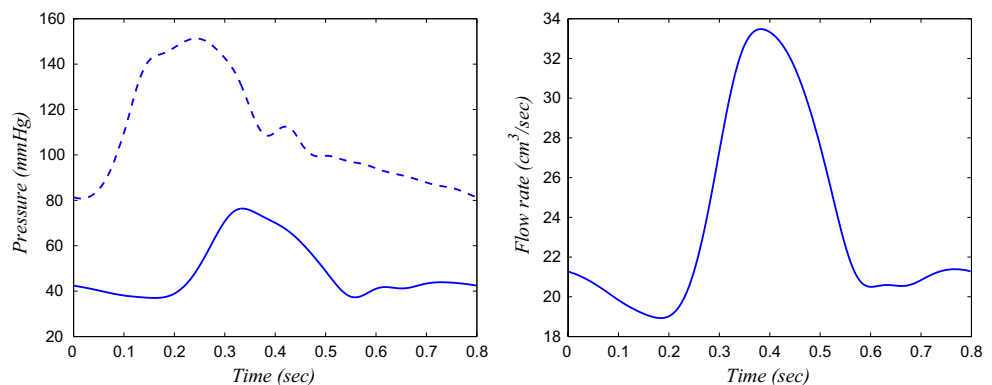
additional branch, p_{inj}, is provided by the SPH simulation. This ensures that the rate of blood loss through the injury, $Q_{inj}(t)$, is moderated by the accumulation of blood within the surrounding tissue. The injury pressure, p_{inj}, and pulsatile rate of blood loss signal, $Q_{inj}(t)$, are exchanged between the SPH and tree model and adjusted once per cardiac cycle.

For visualization purposes, the results of the SPH simulations of bleeding are post-processed using Houdini® 3D animation software. This software automatically creates local surfaces from the collection of SPH particles in each frame and tracks them over time. More specifically, Open-VDB [23] is adopted to sample a high-resolution signed distance field that wraps around all the particles. We further perform five iterations of mean curvature flow smoothing to diminish high-frequency reconstruction noise. A triangulated surface is then generated from the signed distance field with a standard Marching Cubes algorithm. We render the results using Houdini®'s physics-based Mantra ray tracer for visual realism.

3 Results

In this section, the simulation sequence described in the previous section is applied to a specific problem: an injury of a single ballistic projectile passing through the lower left leg, in which the anterior tibial artery has been severed. The pressure at the entrance of the aorta is depicted in the left panel of Fig. 4. This signal is transmitted to the injured artery, as shown in the same panel, with smaller amplitude and a slight delay in the peak pressure. The initial rate of blood loss, shown in the right panel of Fig. 4, is quite severe. However, this rate progressively decreases as the pressure in the injury region rises due to the accumulation of blood in the surrounding tissue. Note that our current vascular tree model does not include effects of vasospasm or autonomic regulation.

The SPH simulation of hemorrhage starts with volume flow rate signal shown in the right panel of Fig. 4. As shown in the upper left panel in Fig. 5, blood starts to expand radially from the injury site through the porous tissue, driven by the pressure difference but resisted by viscous effects and the porosity of the tissue. As can be seen in the subsequent panels, the blood is successfully prevented from penetrating the bone and the skin through the representation of these materials as stationary SPH particles. As blood fills the surrounding soft tissue, pressure in this region rises, thereby reducing the transport into this region. The blood particles are naturally channeled through the least resistive path created by the ballistic exit wound in the
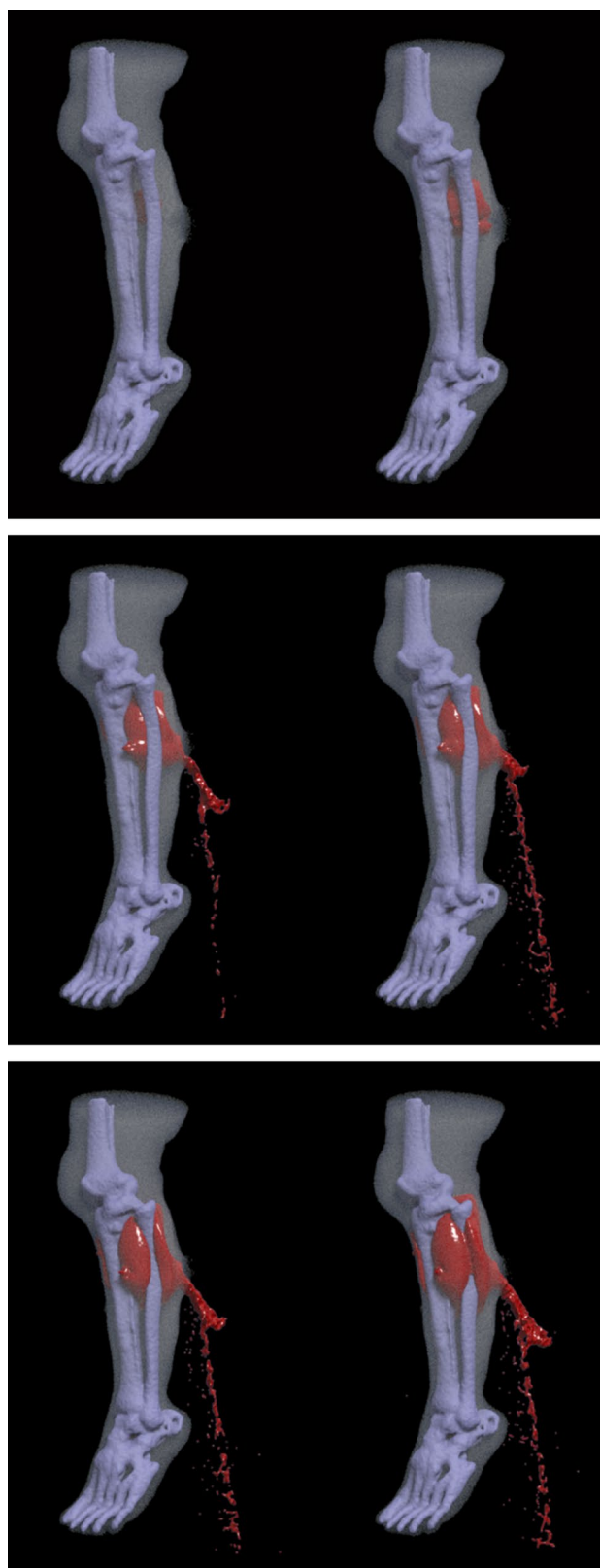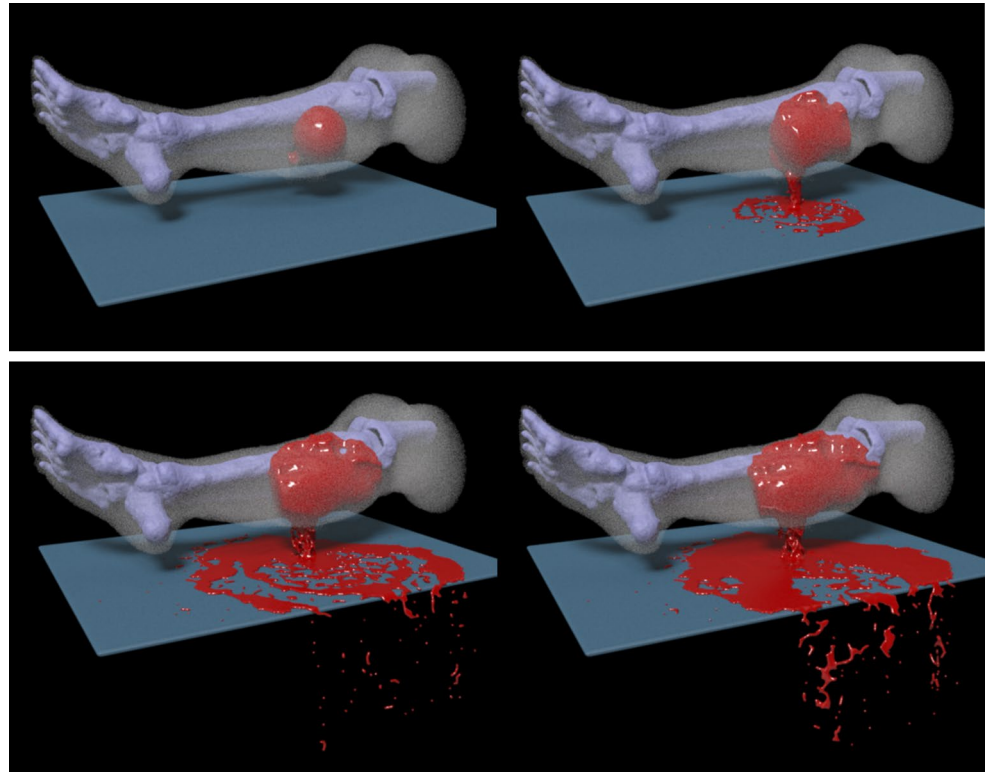

Fig. 5 Hemorrhage of injured left lower leg

Fig. 6 Hemorrhage of injured left lower leg above an impenetrable platform

internal tissue. This wound also has a local void in the skin, where the skin particles are sufficiently dispersed that they cannot maintain an impenetrable barrier to the blood particles. Thus, the blood is ejected out of the leg through the puncture in the skin. It is important to note that there is also a small breach in the skin near the entrance wound, but its size is smaller than the exit wound, and therefore, its large resistance prevents significant blood loss from that site.

The resulting jet from the exit wound is pulsatile, a reflection of the driving signal in the injured artery. The jet falls downward under the influence of gravity. Though surface tension is not explicitly included in the model, there is nonetheless an inherent tendency in the SPH model for the jet to break up and form droplets. It is also important to note that blood particles that leave the leg are unable to repenetrate the skin. Thus, the simulation faithfully captures several important physical effects.

In the previous result, the leg was vertical and removed from other walls or obstacles. In contrast, in the simulation whose results are depicted in Fig. 6, the leg is situated horizontally, just above an impenetrable platform (represented by stationary SPH particles, similar to bone and skin). In this case, the jet impacts the wall and creates a pool that spreads radially outward along the platform. The pool disperses somewhat nonphysically due to a lack of sufficient particle density.

4 Discussion

The integration of physics-based computational techniques enables the simulated generation of injury and physiological hemorrhage in a targeted portion of the human body. By applying distinct properties to the various media—tissue, bone, skin—the depicted results indicate a dispersion of blood through muscular tissue and natural massive bleeding through punctured skin. The bleeding reflects the pulsatile driving signal obtained from the systemic arterial tree model, as shown in Figs. 5 and 6. This hemorrhage behavior is similar to the simulation of bleeding out of an injured arterial vessel by Müller et al. [22]. However, our current simulation is distinguished from the works of Müller et al. [22] by our inclusion of an inflow condition at the injury site obtained from the tree model and by our treatment of a solid boundary wall as a collection of impermeable solid particles, which enables a physically faithful and computationally efficient hemorrhage simulation. Moreover, without the addition of a surface tension force, which is contained in the works of Müller et al. [22], our SPH simulation can still demonstrate natural break up of the liquid jet and free surface of fluid boundary.

The hemorrhage simulation performed in this work is conducted after the injury simulation is completed, under

the assumption that the injury site remains stationary while bleeding progresses. This is a reasonable approach under the condition that time scale of injury generation is much shorter than that of hemorrhage. However, for the purpose of realistic hemorrhage simulation, the simulations of injury and hemorrhage should be conducted simultaneously. This would also enable an account for tissue swelling, which is currently absent. Moreover, the inflow boundary condition from the tree model is obtained from a periodic cycle of the pressure signal in the aorta, as shown in Fig. 4, which does not account for transient pressure drop from the loss of blood. Severe loss of blood can lead to emergent medical conditions such as hypovolemic shock, unconsciousness and failure of organs, which require immediate medical attentions. Therefore, there should be feedback of the instantaneous total blood volume and some degree of autonomic regulation in order to correctly account for the blood loss and its accompanying transient effects on the cardiac cycle and vasospasm. Finally, the current study does not include a model for the coagulation cascade, which would be important on both short and long time scales to simulate a natural response to vascular injury.

In our ongoing study, we are extending the work presented in this paper to include many of these aforementioned effects. For example, by coupling the MPM and SPH simulations, the geometric changes to the injury site—such as swelling—will be accounted for in the hemorrhage visualization. Moreover, the fidelity of the local physiological conditions—particularly, the rate of bleeding—can be improved by simultaneously simulating the conditions in the systemic cardiovascular network. This network simulation is closed with the feedback from the autoregulatory function, thereby accounting for the natural response to progressive loss of blood volume. Furthermore, we are exploring computational strategies—such as by using machine learning tools, in which the physical behaviors of fluid and solid particles are estimated from large training sets of pre-computed data—that will accelerate the overall simulation time toward real-time visualization.

5 Conclusions

A sequence of physics-based simulation techniques has been developed to simulate traumatic injury and bleeding in the human body. This sequence utilizes, for the first time, a high-fidelity simulation of bleeding coupled with a tree model of the systemic circulation in order to provide realistic inflow conditions at the site of the injury. The overall approach has been demonstrated on a ballistic projectile injury to the lower leg and the subsequent hemorrhage over a short interval. We anticipate the improved physics-based simulation techniques can provide an essential tool for future medical training such as virtual surgery.

**Compliance with ethical standards**

Conflict of interest The authors declare that they have no conflict of interest.

Ethical approval All procedures performed in studies involving human participants were in accordance with the ethical standards of the institutional and/or national research committee and with the 1964 Helsinki Declaration and its later amendments or comparable ethical standards.

References

1. Akinci N, Ihmsen M, Akinci G, Solenthaler B, Teschner M (2012) Versatile rigid-fluid coupling for incompressible SPH. ACM Trans Graph 31(4), Art ID 62. doi:10.1145/2185520.2185558
2. Avolio AP (1980) Multi-branched model of the human arterial system. Med Biol Eng Comput 18(6):709–718
3. Basdogan C, Ho C-H, Srinivasan MA (2001) Virtual environments for medical training: graphical and haptic simulation of laparoscopic common bile duct exploration. IEEE/ASME Trans Mechatron 6(3):269–285
4. Boisvert J, Poirier G, Borgeat L, Godin G (2013) Real-time blood circulation and bleeding model for surgical training. IEEE Trans Biomed Eng 60(4):1013–1022
5. Bridson R (2007) Fast poisson disk sampling in arbitrary dimensions. In: ACM SIGGRAPH 2007 Sketches. SIGGRAPH ' 07:2007
6. Courtecuisse H, Allard J, Kerfriden P, Bordas SP, Cotin S, Duriez C (2014) Real-time simulation of contact and cutting of heterogeneous soft-tissues. Med Image Anal 18(2):394–410
7. Dehnen W, Aly H (2012) Improving convergence in smoothed particle hydrodynamics simulations without pairing instability. Mon Not R Astron Soc 425(2):1068–1082
8. Desbrun M, Gascuel MP (1996) Smoothed particles: a new paradigm for animating highly deformable bodies. In: Computer animation and simulation '96 proceedings of EG workshop on animation and simulation. Springer, pp 61–76
9. Durlofsky L, Brady JF (1987) Analysis of the brinkman equation as a model for flow in porous media. Phys Fluids 30:3329–3341
10. Frank P, Eldredge JD, Benharash P, Dutson EP (2016) Real-time numerical simulation of the cardiovascular system and autoregulatory mechanisms in response to hemorrhagic injury. In: Preparation
11. Gallagher AG, Ritter EM, Champion H, Higgins G, Fried Marvin P, Moses Gerald, Smith C Daniel, Satava Smith (2005) Virtual reality simulation for the operating room: proficiency-based training as a paradigm shift in surgical skills training. Ann Surg 241(2):364–372
12. Gingold RA, Monaghan JJ (1977) Smoothed particle hydrodynamics: theory and application to non-spherical stars. MNRAS 181:375–389
13. Horvath CJ, Solenthaler B (2013) Mass preserving multi-scale sph. In: Pixar Technical Memo 13-04, Pixar Animation Studios

14. Jiang C, Schroeder C, Selle A, Teran J, Stomakhin A (2015) The affine particle-in-cell method. ACM Trans Graph 34(4):51:1–51:10

15. Kellman J (2014) Adaptive response-time-based category sequencing in perceptual learning. Vis Res 99:111–123

16. Krasne S, Hillman JD, Kellman PJ, Drake TA et al (2013) Applying perceptual and adaptive learning techniques for teaching introductory histopathology. J Pathol Inform 4(1):34

17. Kühnapfel U, Cakmak HK, Maaß H (2000) Endoscopic surgery training using virtual reality and deformable tissue simulation. Comput Graph 24(5):671–682

18. Liu A, Tendick F, Cleary K, Kaufmann C (2003) A survey of surgical simulation: applications, technology, and education. Presence Teleoperators Virtual Environ 12(6):599–614

19. Lucy LB (1977) Numerical study of liquid composite molding using a smoothed particle hydrodynamics method. Astron J 82:1013–1024

20. Meier U, López O, Monserrat C, Juan MC, Alcaniz M (2005) Real-time deformable models for surgery simulation: a survey. Comput Methods Programs Biomed 77(3):183–197

21. Müller M, Charypar D, Gross M (2003) Particle-based fluid simulation for interactive applications. In: Proceedings of the 2003 ACM SIGGRAPH/Eurographics symposium on computer animation

22. Müller M, Schirm S, Teschner M (2003) Interactive blood simulation for virtual surgery based on smoothed particle hydrodynamics. Technol Health Care 12:25–31

23. Museth K (2014) A flexible image processing approach to the surfacing of particle-based fluid animation (invited talk). In: Mathematical progress in expressive image synthesis I, volume 4 of mathematics for industry, pp 81–84

24. Oger Guillaume, Doring Mathieu, Alessandrini Bertrand, Ferrant Pierre (2007) An improved sph method: Towards higher order convergence. Journal of Computational Physics 225(2):1472–1492

25. Ram D, Gast T, Jiang C, Schroeder C, Stomakhin A, Teran J, Kavehpour P (2015) A material point method for viscoelastic fluids, foams and sponges. In: Proceedings of the 14th ACM SIGGRAPH / Eurographics symposium on computer animation, SCA '15, pp 157–163

26. Solenthaler B, Gross M (2011) Two-scale particle simulation. In: Proceedings of ACM SIGGRAPH 30:2011

27. Stam J, Fiume E (1995) Depicting fire and other gaseous phenomena using diffusion processes. In: Proceedings of the 22nd annual conference on computer graphics and interactive techniques, pp 129–136. ACM

28. Stergiopulos N, Young DF, Rogge TR (1992) Computer simulation of arterial flow with application to arterial and aortic stenoses. J Biomech 25(12):1477–1488

29. Stomakhin A, Schroeder C, Chai L, Teran J, Selle A (2013) A material point method for snow simulation. ACM Trans Graph 32(4):1021–10210

30. Stomakhin A, Schroeder C, Jiang C, Chai L, Teran J, Selle A (2014) Augmented MPM for phase-change and varied materials. ACM Trans Graph 33(4):138:1–138:11

31. Su D, Ma R, Zhur L (2011) Numerical study of liquid composite molding using a smoothed particle hydrodynamics method. Special Top Rev Porous Media Int J 2(3):205–212

32. Sulsky D, Zhou S-J, Schreyer HL (1995) Application of a particle-in-cell method to solid mechanics. Comput Phys Commun 87(1–2):236–252

33. Womersley JR (1957) Oscillatory flow in arteries: the constrained elastic tube as a model of arterial flow and pulse transmission. Phys Med Biol 2:178–187
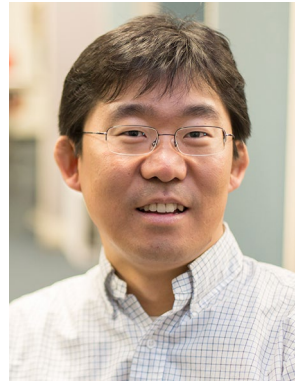
Kwitae Chong is a Postdoctoral Research Associate in the Mechanical & Aerospace Engineering Department at UCLA. His research involves theoretical and computational research of fluid dynamics and biological problems and biomedical flows.

Chenfanfu Jiang received his Ph.D. in Computer Science at UCLA in 2015, awarded Edward K. Rice Outstanding Doctoral Student. He is currently a postdoc at UCLA working on solid/fluid mechanics.


Daniel Ram earned his Ph.D. in mathematics from the University of California, Los Angeles in 2015. His research interests include computational solid and fluid mechanics and numerical analysis.

Anand Santhanam is an AssistantProfessor of Radiation Oncology at UCLA. His research involvesapplying new technology to radiation therapy, specifically in thearea of 3D surface imaging and tissue biomechanics modeling.

Demetri Terzopoulos isDistinguished Professor and Chancellor's Professor of ComputerScience at UCLA. His research involves computer graphics, computervision, medical image analysis, computer-aided design and artificialintelligence/life.
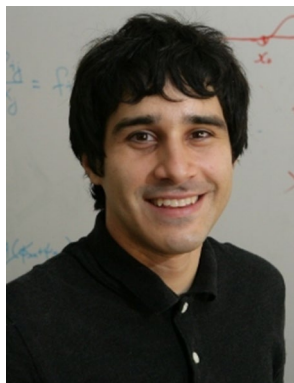
Joseph Teran is a Professor ofapplied mathematics at UCLA. His research focuses on numericalmethods for partial differential equations in classical physics,including computational solids and fluids, multi-materialinteractions, fracture dynamics and computational biomechanics.

Peyman Benharash is an AssistantProfessor of Surgery at the UCLA School of Medicine and acardiothoracic surgeon. His research group is diverse andspecializes in hemodynamic modeling, development of surgicalsimulators, and cardiovascular tissue engineering.

Jeff D. Eldredge is a Professor in theMechanical \& Aerospace Engineering Department at UCLA. His researchinvolves theoretical and computational investigations of fluiddynamics, including biomedical flows, unsteady aerodynamics, andbiological locomotion.

Erik Dutson is an AssociateProfessor of Surgery, General Surgery and Executive Medical Directorof Center for Advanced Surgical and Interventional Technology(CASIT) at UCLA. His research involves computer-assisted, roboticsurgery and clinical management of obesity.